MATERIALS SCIENCE

Disorder-order transition–induced unusual bandgap bowing effect of tin-lead mixed perovskites

Han Gao[1]†, Dong He[1]†, Zehua Chen[2]†, Peili Gao[3]†, Dongsheng He[4]†, Zhaoning Li[1], Xusheng Zhang[1], Jingwei Xiu[1], Qiang Sun[1], Shuming Chen[3], Su-Huai Wei[5]*, Shu-Hong Yu[1,6], Zhubing He[1,6]*

Owing to the predominant merit of tunable bandgaps, tin-lead mixed perovskites have shown great potentials in realizing near-infrared optoelectronics and are receiving increasing attention. However, despite the merit, there is still a lack of fundamental understanding of the bandgap variation as a function of Sn/Pb ratio, mainly because the films are easy to segregate in terms of both composition and phase. Here, we report a fully stoichiometric synthesis of monocrystalline $FAPb_{1-x}Sn_xI_3$ nanocrystals as well as their atomic-scale imaging. On the basis of the systematic measurements of the monocrystalline materials, strain and Coulomb interaction–induced atomic ordering was revealed to be responsible for the unusual discontinuous bandgap jumping near $x = 0.5$ from the expected bowing effect. As a result, both $FAPb_{0.6}Sn_{0.4}I_3$ and $FAPb_{0.4}Sn_{0.6}I_3$ have the lowest bandgaps of around 1.27 electron volts, while that of $FAPb_{0.5}Sn_{0.5}I_3$ is 1.33 electron volts. Correspondingly, their based light-emitting diodes can emit infrared lights with the wavelengths reaching 930 nanometers.

INTRODUCTION

Tin-lead mixed perovskites (TLPs) show great potential in optoelectronics and turn to be one of the most promising future materials owing to their tunable optical bandgaps as low as 1.25 eV (*1*, *2*), along with reduced usage of toxic lead. These allow TLPs to be considered in broad optoelectronic applications such as solar cells (*3*, *4*), near-infrared photodetectors (*5*), and light-emitting sources (*6*). However, the study on the structure-property relationship of the promising TLP materials is still at its early stage (*7*–*9*), especially on the atomic arrangement of Sn/Pb in the alloy, and deserves extensive explorations. One of the biggest obstacles is to see their atomic arrangement in the lattices. Although some atomic lattice images of sensitive organic-inorganic hybrid perovskites were reported in the past (*10*, *11*), tin halide–based perovskites have never been successfully recorded. Besides suffering from the electronic and thermal damage of electron beam (EB) in transmission electron microscopy (TEM) (*12*–*14*), the easy delocalization of the $5s^2$ electrons of Sn^{2+} ions in the lattice under the influence of the ambient environment makes the visualization of TLP lattices an insurmountable challenge (*15*).

With limited atomic imaging, there is lack of fundamental insight and full-scope understanding of Sn/Pb ratio–dependent optical bandgaps for TLP materials (*16*, *17*). From an experimental point of view, those synthesized polycrystalline TLP films suffer from inevitable phase and composition segregations because of different crystallization rates between tin and lead perovskites (*18*, *19*). On the other hand, monocrystalline TLP nanocrystals provide a superior platform to study the structure-property relationship for this type of material. This is because TLP nanocrystals capped with surficial ligands are more stable and are able to endure the EB attack in the atomic imaging process (*20*). Recently, some exceptional optical properties such as multiple exciton generation of TLP nanocrystals were found (*21*), but the report has a very limited composition range and no clear exhibition of atomic structures. Therefore, the synthesis of fully stoichiometric and monocrystalline TLP nanocrystals is critical to study the structure-property relationship of this system.

Regarding the relationship, for most semiconductor alloys $A_{1-x}B_x$, the bandgap usually varies with alloy composition x following the bowing relationship, i.e., $E_g(x) = (1 - x)E_g(A) + xE_g(B) - bx(1 - x)$, where b is the so-called bowing parameter. Although the TLP bandgap bowing has been observed in $FAPb_{1-x}Sn_xI_3$ (*22*–*26*), so far, there is no underlying physical explanation why the bandgap of $Sn_{0.5}Pb_{0.5}$-based TLP obviously jumps away from the expected values of bowing curves as a function of the Sn/Pb ratio (*24*, *25*). Therefore, it is important to reveal the physical mechanism to explain this puzzling behavior and contributing to the semiconductor alloy physics.

To address three essential issues, in this work, we report a fully stoichiometric synthesis of monocrystalline $FAPb_{1-x}Sn_xI_3$ nanocrystals and their atomic-scale lattice imaging. The difficulty in recording the atomic lattice of tin-based perovskites was surmounted in this work by cryo-TEM. On the basis of that critical platform, we reveal that the disorder to order of Sn/Pb positioning in the TLP lattice accounts for that jumping point at $FAPb_{0.5}Sn_{0.5}I_3$. As revealed by first-principles density functional theory calculations and correlated characterized evidence, the ordering of Sn/Pb positioning in the TLP lattice reduces the strain and yields considerable Coulomb energy gain, which markedly lowers the mixing enthalpy. The enhanced coupling between the unoccupied conduction bands and occupied valence bands leads to a larger bandgap in the ordered $FAPb_{0.5}Sn_{0.5}I_3$, deviating notably from the expected bowing curve. As a result, the reddest band edge absorptions of our TLP nanocrystals occur around 975 nm for both $FAPb_{0.6}Sn_{0.4}I_3$

[1]Department of Materials Science and Engineering, Shenzhen Key Laboratory of Full Spectral Solar Electricity Generation (FSSEG), Southern University of Science and Technology, No. 1088, Xueyuan Rd., Shenzhen 518055, Guangdong, China. [2]Beijing Computational Science Research Center, Beijing 100193, China. [3]Department of Electrical and Electronic Engineering, Southern University of Science and Technology, No. 1088, Xueyuan Rd., Shenzhen 518055, Guangdong, China. [4]Core Research Facilities, Southern University of Science and Technology, No. 1088, Xueyuan Rd., Shenzhen 518055, Guangdong, China. [5]Eastern Institute of Technology, Ningbo 315200, China. [6]Guangdong Provincial Key Laboratory of Sustainable Biomimetic Materials and Green Energy, Southern University of Science and Technology, No. 1088, Xueyuan Rd., Shenzhen 518055, China.
*Corresponding author. Email: hezb@sustech.edu.cn (Z.H.); suhuaiwei@eitech.edu.cn (S.-H.W.)
†These authors contributed equally to this work.

and $FAPb_{0.4}Sn_{0.6}I_3$, while that of $FAPb_{0.5}Sn_{0.5}I_3$ is around 930 nm. As a device of concept, we built three kinds of infrared light-emitting diodes (LEDs) on the basis of $FAPb_{0.6}Sn_{0.4}I_3$, $FAPb_{0.5}Sn_{0.5}I_3$, and $FAPb_{0.4}Sn_{0.6}I_3$ with emission wavelengths of 919, 915, and 930 nm, respectively.

RESULTS

Fully stoichiometric synthesis of TLP nanocrystals

TLP nanocrystals were synthesized with a modified hot-injection method (*27*) by injecting formamidinium oleate into a mixed precursor solution of lead iodide (PbI_2) and tin iodide (SnI_2) in octadecene in an inert atmosphere (see Materials and Methods for details), where oleic acid (OAc), oleylamine (OLA), and tri-*n*-octylphosphine (TOP) were used as ligands. ^{1}H nuclear magnetic resonance (NMR) (fig. S1) and Fourier transform infrared (FTIR) spectra (Fig. 1A) show that OLA and TOP may cap firmly on the surface of TLP nanocrystals along with OAc (*28*). The interactions of OLA-$PbI_2(SnI_2)$ and TOP-$PbI_2(SnI_2)$ are confirmed by the movements of signatures of OLA (—NH_2; 1622 cm^{-1}) and TOP (C—P; 1028, 1113, and 1186 cm^{-1}), while OAc shows a negligible shift (fig. S2). OAc is responsible for dissolving formamidinium acetate to synthesize formamidinium oleate, acting possibly as a steric effect in the purified nanocrystal solution. X-ray photoelectron spectroscopy (XPS) examines the existence of both divalent Pb and Sn in the TLP nanocrystals (Fig. 1B and fig. S3) with the Sn:Pb atomic ratio calculated at 2.10:2.21 (table S1) and herein marked as $FAPb_{0.5}Sn_{0.5}I_3$, although the input ratio of SnI_2:PbI_2 is 9:1. The big contrast of Sn:Pb ratio demonstrates that the real Sn:Pb ratio formed in the crystals is distinct from the input one in the precursor solution (*20*), which was neglected and hardly investigated especially in a thin film (*29*).

To reveal the relationship between the real and input Sn:Pb ratios, we carried out a fully stoichiometric synthesis of $FAPb_{1-x}Sn_xI_3$ nanocrystals with x varying from 0 to 1. Depending on inductively coupled plasma mass spectrometry (ICP-MS), the real Sn:Pb ratio of each kind of TLP nanocrystal was determined, which is summarized in Fig. 1C. This work reports the fully stoichiometric synthesis of $FAPb_{1-x}Sn_xI_3$ nanocrystals. It is impressive that the input ratio of Sn:Pb is much larger than the final one for each stoichiometric TLP nanocrystal. That may be attributed to the slow tin release rate due to the strong dative bond strength of the Sn-TOP complex (*30*). In addition, TOP is indispensable to form TLP nanocrystals in the hot-injection system because the mixed powder of PbI_2 and SnI_2 cannot dissolve completely in the solvents without TOP (fig. S2).

Then, x-ray diffraction (XRD) was used to determine the phase structure of our TLP nanocrystals (Fig. 1D). Figure 1E shows that all the TLP nanocrystals have a cubic phase, following the standard JCPDS (Joint Committee on Powder Diffraction Standards) patterns of $FAPbI_3$ (light green) (*31*) and $FASnI_3$ (wine) (*32*) shown at the bottom. That excludes the existence of such tetravalent tin as FA_2SnI_6 owing to suppressing oxidation by capped OLA and TOP ligands. We also observe the obvious lattice variation from full lead to full tin in the magnified (002) peak because (002) is attributed to the lattice size of the octahedral cage in the perovskite structure (Fig. 1F). As the content of smaller-size Sn atom increases, that lattice size of the (001) plane shrinks successively from full lead and

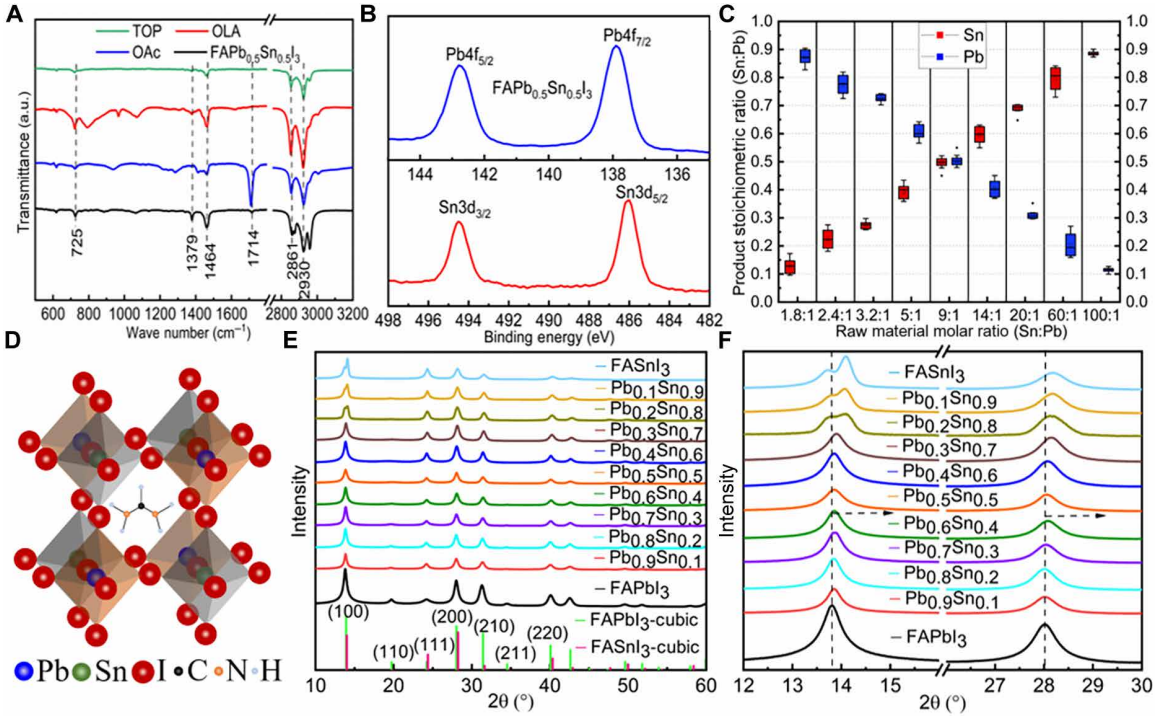

Fig. 1. Characterizations of $FAPb_{1-x}Sn_xI_3$ nanocrystals. (**A**) FTIR spectra of $FAPb_{0.5}Sn_{0.5}I_3$ nanocrystals and capping ligands of OAc, OLA, and TOP. a.u., arbitrary units. (**B**) XPS of Pb 4f and Sn 3d of $FAPb_{0.5}Sn_{0.5}I_3$ nanocrystals. (**C**) ICP-MS of $FAPb_{1-x}Sn_xI_3$ nanocrystals. (**D**) Crystal structure of the cubic-phase $FAPb_{0.5}Sn_{0.5}I_3$ nanocrystals. (**E**) XRD patterns of $FAPb_{1-x}Sn_xI_3$ nanocrystals. (**F**) Enlarged view of the XRD patterns at low angles.

full tin, which follows the downsizing of the octahedral cage shown at 28° after substituting lead by tin. Another phenomenon is the split peaks from $Pb_{0.2}Sn_{0.8}$ to full tin, which may be attributed to the lattice-shared octahedra with differentiated tilting angles when increasing x in $Pb_{1-x}Sn_x$ (*22*, *27*).

Figure 2 shows the uniform morphologies of all the fully stoichiometric TLP nanocrystals visualized by TEM with a narrow size distribution and an average size around 15 nm, which were synthesized at a reaction temperature of 80°C for 5 s. In the hot-injection route, the temperature also plays a crucial role in determining the final size of TLP nanocrystals. To normalize the same average size for each kind of TLP nanocrystal, we synthesized the $FASnI_3$ nanocrystals with a size of 15 nm at 100°C (Fig. 2L), while their average size would be 11 nm with the synthesis temperature of 80°C (Fig. 2K). Moreover, all the TLP nanocrystals show good crystallinity. Those above examine the effectiveness of our fully stoichiometric synthesis method.

Atomic lattice images recorded by cryo-TEM

Compared with the above low-magnification TEM ones, it is much harder to obtain atomic lattice images of sensitive metal-halide perovskite materials. The soft lattices of the perovskite materials suffer from damages and amorphization in the imaging and herein need the electron dose and accelerating voltage as low as possible, along with short-exposure time (*13*). In contrast to lead perovskite, tin halide perovskites would be much weaker because of the obvious structure change as a result of the oxidation of tin from divalent to tetravalent (*33*). As far as we know, atomic lattice images of tin halide–based perovskite materials are never reported so far. In this work, we report the atomic lattice images of all TLP nanocrystals using cryo-TEM by controlling the EB dose of ~2.2 e $Å^{-2}$ s^{-1} for 8 s with Gatan electron-counting direct detectors (Fig. 3). The corresponding fast Fourier transformation patterns were indexed to be a cubic phase along the $[100]_T$ zone axis. The successful image recording can be attributed partially to the easier zone-axis alignment of monodisperse and small-size TLP nanocrystals with various crystal planes exposed (fig. S4) than continuous perovskite films and large-size crystals.

Figure 3A exhibits unambiguously a typical atomic lattice image of (100) plane enlarged from the red frame marked in Fig. 3D, where Pb (Sn) and I atoms can be identified even along with the information of formamidinium. Depending on the exit-wave reconstruction, the atoms in the lattice can be unambiguously identified (Fig. 3B). This shows that no point and line defects ever appeared in the previous report (*34*). The image fits well in the perovskite lattice scheme and is much clearer than our former report (*35*). The lattice would be damaged and lastly amorphized when increasing the exposure time (fig. S5). Our successful image-catching ability relies heavily on the image-seizing speed under the dose threshold of ~2.2 e $Å^{-2}$ s^{-1}. Depending on the exposure technique, as fast as we can, the atomic lattice images of TLP nanocrystals with typical Pb/Sn ratios were successfully collected, including $FAPb_{0.7}Sn_{0.3}I_3$, $FAPb_{0.6}Sn_{0.4}I_3$, $FAPb_{0.5}Sn_{0.5}I_3$, $FAPb_{0.4}Sn_{0.6}I_3$, $FAPb_{0.3}Sn_{0.7}I_3$, and $FASnI_3$, shown respectively in Fig. 3 (C to F). However, we failed in seizing the images of corresponding TLP films under the same conditions, which proves the higher stability of TLP nanocrystals than films under the EB attack. According to our observations in TEM recording, that can be attributed to their lattices enhanced by surface ligands besides the higher crystallinity of nanocrystals.

Order-disorder phase transition disrupts the gradual TLP bandgap variation

Regarding the bandgap bowing effect, we normalized the average size of all the stoichiometric TLP nanocrystals at 15 nm (Fig. 2) and far beyond the Bohr radii of both $FAPbI_3$ (6.1 nm) (*36*) and $FASnI_3$ (3.5 to 4.4 nm) (*37*) to exemplify the size quantum effect. All TLP nanocrystals belong to cubic phases and herein exclude the influence of phase variation (Fig. 1E).

Figure 4A shows the absorption edges derived from the absorption spectra for $FAPb_{1-x}Sn_xI_3$ nanocrystals at different compositions. For the Pb-rich compositions (Sn contents $x < 0.5$), the absorption edge rises from 808 to 970 nm with increasing Sn contents. For the Pb-poor compositions (Sn contents $x > 0.5$), increasing Sn content leads to a blue shift of the absorption edge starting from 966 to 821 nm. Notably, for equivalent Pb and Sn contents at $x = 0.5$, the absorption edge appears at 930 nm, lower than the nearest-neighboring compositions considered at $x = 0.4$ and 0.6. The bandgaps calculated for all considered compositions are shown in Fig. 4B and table S2. Their bandgaps extracted from the peak wavelength of all TLP nanocrystals' photoluminescence (PL) spectra also form a bowing curve with $FAPb_{0.5}Sn_{0.5}I_3$ jumping out (fig. S6), consistent with that obtained from the absorption spectra (Fig. 4B). The $FAPbI_3$ nanocrystal exhibits the widest optical bandgap of 1.53 eV, which is identical to the value reported for its corresponding thin film (*38*), while for the $FASnI_3$ nanocrystal, it has a bandgap of 1.51 eV, considerably higher than the bandgap of 1.38 eV for its thin film (*39*). The latter may be correlated to the split (001) peak in its XRD pattern (Fig. 1F) and herein be ascribed to the quantum confinement effect of lattice-shared $[SnI_6]^{4-}$ octahedra with differentiated tilting angles (*22*, *27*, *40*). Except for $FAPb_{0.5}Sn_{0.5}I_3$, the TLP nanocrystals display bowing in the bandgap with the bowing parameter b of 0.94, following the quadratic fitting rule $E_g(x) = xE_g(x = 1) + (1 - x)E_g(x = 0) - bx(1 - x)$. A consensus has been currently drawn that structural relaxation is responsible for the observed bandgap bowing of TLP perovskites (*41*). However, the bandgap of $FAPb_{0.5}Sn_{0.5}I_3$ is positioned above the bottom of the curve, breaking the quadratic rule. This is different from what is observed for the bowing character of some reported $FAPb_{1-x}Sn_xI_3$ films (*8*, *9*, *22*, *24*, *27*), as well as the TLP films we fabricated (fig. S7). This distinct finding for Pb-Sn alloy at $x = 0.5$ has also been seen in some calculations and experiments (*24*, *26*). However, the understanding is still lacking.

As Fig. 4C shows, the Sn/Pb ratio–dependent feature of the TLP nanocrystal microstrains agrees well with the bowing trend of bandgaps, which was calculated from the slope of the linear fitting (fig. S8) and extracted from the broad peak of lattice planes (Fig. 1F), depending on the Williamson-Hall method (*42*, *43*). The TLP nanocrystals experience an increased (decreased) microstrain with increasing Sn concentrations for $x < 0.5$ ($x > 0.5$), leaving the composition at $x = 0.5$ departing obviously from the established trend with a comparable microstrain as the pure $FAPbI_3$ and $FASnI_3$ compounds. Compared with TLP nanocrystals, the microstrains of the corresponding TLP films are mixed approximately within the range of 0.4 to 0.5 (fig. S9). This declares that the strains relax in polycrystalline films but are preserved well in TLP monocrystalline nanocrystals by surficial capping ligands. Figure 4 (D to F) presents the two-dimensional intensity profiles of the three TLP nanocrystal atomic lattices with Pb/Sn ratios of 6:4, 5:5, and 4:6, respectively, extracted from their cryo-TEM images (Fig. 3, D to F). In the atomic lattice images, the iodine-only column has the lowest intensity and acts as the baseline, while the intensity of the Pb (Sn)-I

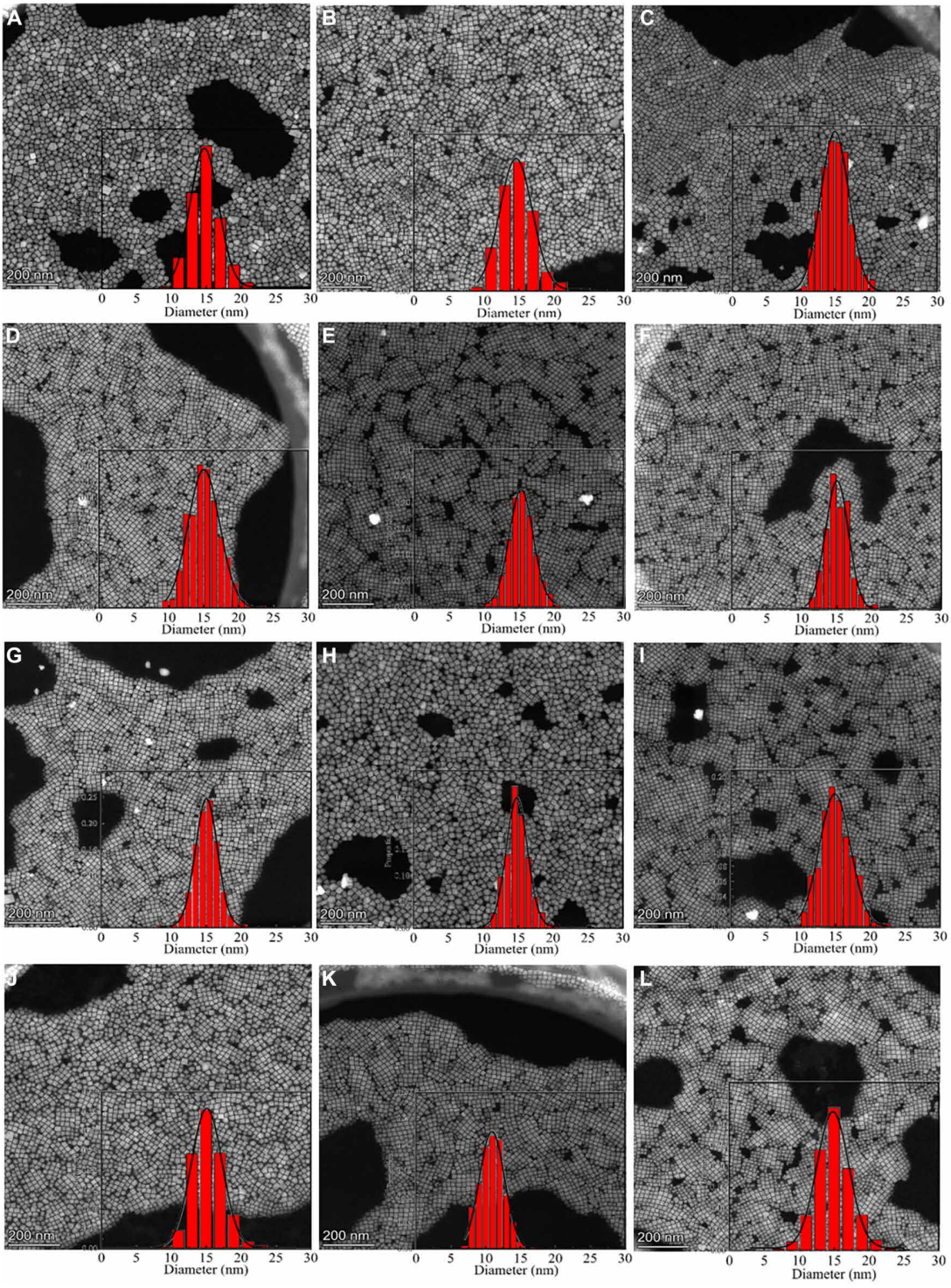

Fig. 2. TEM images of $FAPb_{1-x}Sn_xI_3$ nanocrystals in a low-magnification view with a scale bar of 200 nm. (**A**) $FAPbI_3$, (**B**) $FAPb_{0.9}Sn_{0.1}I_3$, (**C**) $FAPb_{0.8}Sn_{0.2}I_3$, (**D**) $FAPb_{0.7}Sn_{0.3}I_3$, (**E**) $FAPb_{0.6}Sn_{0.4}I_3$, (**F**) $FAPb_{0.5}Sn_{0.5}I_3$, (**G**) $FAPb_{0.4}Sn_{0.6}I_3$, (**H**) $FAPb_{0.3}Sn_{0.7}I_3$, (**I**) $FAPb_{0.2}Sn_{0.8}I_3$, (**J**) $FAPb_{0.1}Sn_{0.9}I_3$, and $FASnI_3$ nanocrystals synthesized at 80°C (**K**) and 100°C (**L**). Inset diagrams are their size distributions.

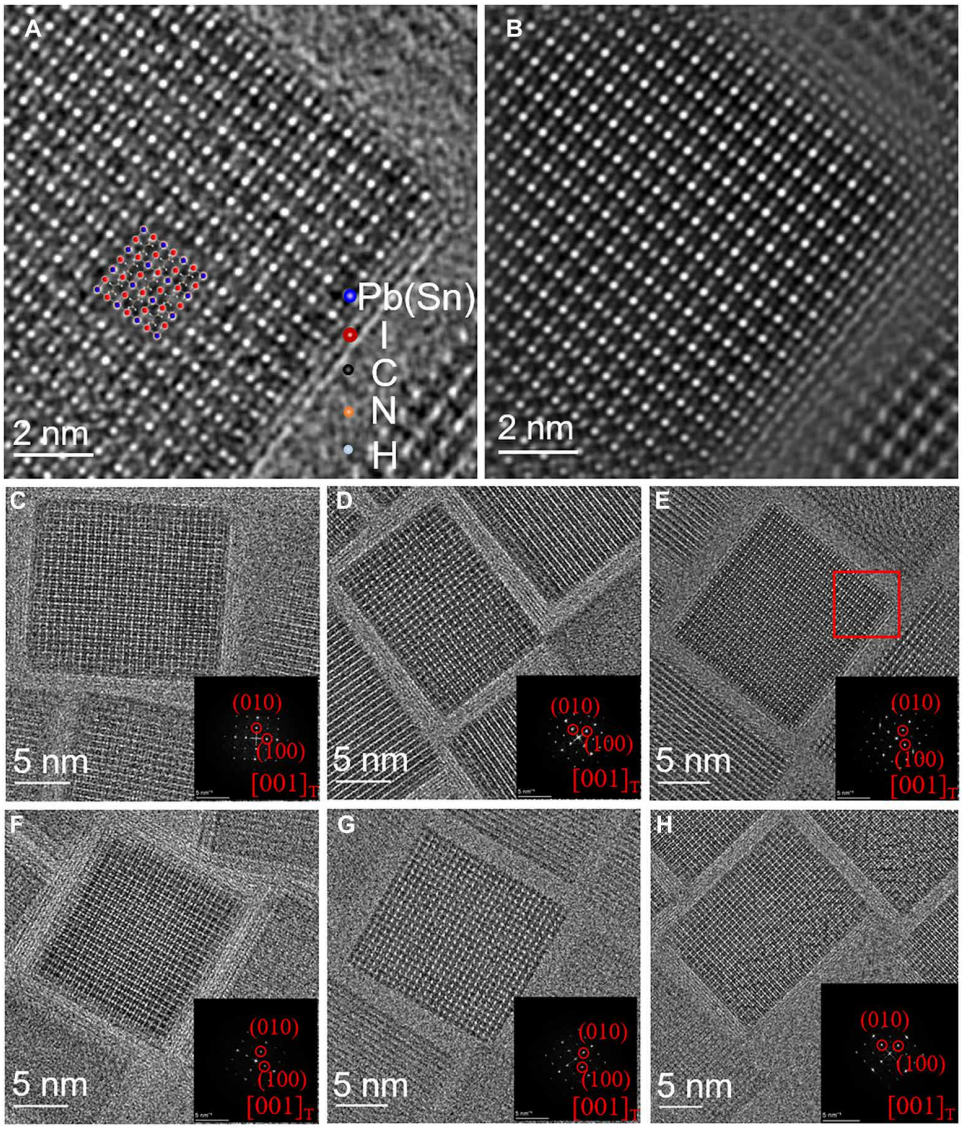

Fig. 3. High-resolution lattice images of $FAPb_{1-x}Sn_xI_3$ nanocrystals via cryo-TEM. (**A**) Magnified atomic-scale lattice image of the red rectangle region marked in that of typical $FAPb_{0.5}Sn_{0.5}I_3$ nanocrystals (E), matched with the molecule structure model. (**B**) Atomic lattice phase image of (A) resolved by exit-wave reconstruction. Representative high-resolution images of (**C**) $FAPb_{0.7}Sn_{0.3}I_3$, (**D**) $FAPb_{0.6}Sn_{0.4}I_3$, (**E**) $FAPb_{0.5}Sn_{0.5}I_3$, (**F**) $FAPb_{0.4}Sn_{0.6}I_3$, (**G**) $FAPb_{0.3}Sn_{0.7}I_3$, and (**H**) $FASnI_3$. In addition, each inset is the corresponding electron diffraction pattern from fast Fourier transformation. f.u., formula unit.

alternative-stacking column varies with the square of the atomic number (fig. S10) (*44*). Here, the statistics of the intensity gaps between the Pb (Sn)-I alternative-stacking column and the baseline allow us to discern the disorder-order change of Pb-Sn positioning in the lattice. As summarized in fig. S11, the average intensity values are 77.79, 72.20, and 81.52 for $FAPb_{0.6}Sn_{0.4}I_3$, $FAPb_{0.5}Sn_{0.5}I_3$, and $FAPb_{0.4}Sn_{0.6}I_3$, respectively. $FAPb_{0.5}Sn_{0.5}I_3$ has the lowest intensity, indicating the existence of Pb-Sn ordering, whereas the Pb-Sn positioning remains disordered in both $FAPb_{0.6}Sn_{0.4}I_3$ and $FAPb_{0.4}Sn_{0.6}I_3$ with higher intensity. The statistical σ values of $FAPb_{0.6}Sn_{0.4}I_3$ (30.96 ± 2.17) and $FAPb_{0.4}Sn_{0.6}I_3$ (41.24 ± 0.70) are much larger than that of $FAPb_{0.5}Sn_{0.5}I_3$ (22.13 ± 0.41), which also proves that the ordering character of $FAPb_{0.5}Sn_{0.5}I_3$ changed from the disordering $FAPb_{0.6}Sn_{0.4}I_3$ and $FAPb_{0.4}Sn_{0.6}I_3$ lattices. Regarding the tested microstrains and the characterized lattice atomic stacking discussed above, the bandgap bowing effect of the TLP bandgap is experimentally validated, especially about the jumping over the bowing for $FAPb_{0.5}Sn_{0.5}I_3$. This indicates that the ordering of Pb-Sn in the lattice may be responsible for the jumping.

To examine the Pb-Sn ordering effect of TLP occurring at $x = 0.5$, we carry out density functional theory calculations, combined with the cluster expansion method as implemented in the Alloy-Theoretic Automated Toolkit (ATAT) code. To reduce the complexity from formamidinium, we used $CsPb_{1-x}Sn_xI_3$ as a prototypical example to search the ground-state ordered structures. The $CsPb_{1-x}Sn_xI_3$ alloy system shows predominantly disordered behaviors with positive mixing enthalpies (fig. S12). However, a remarkable exception is observed at $x = 0.5$ with the ordered atomic structure (fig. S13A), where the

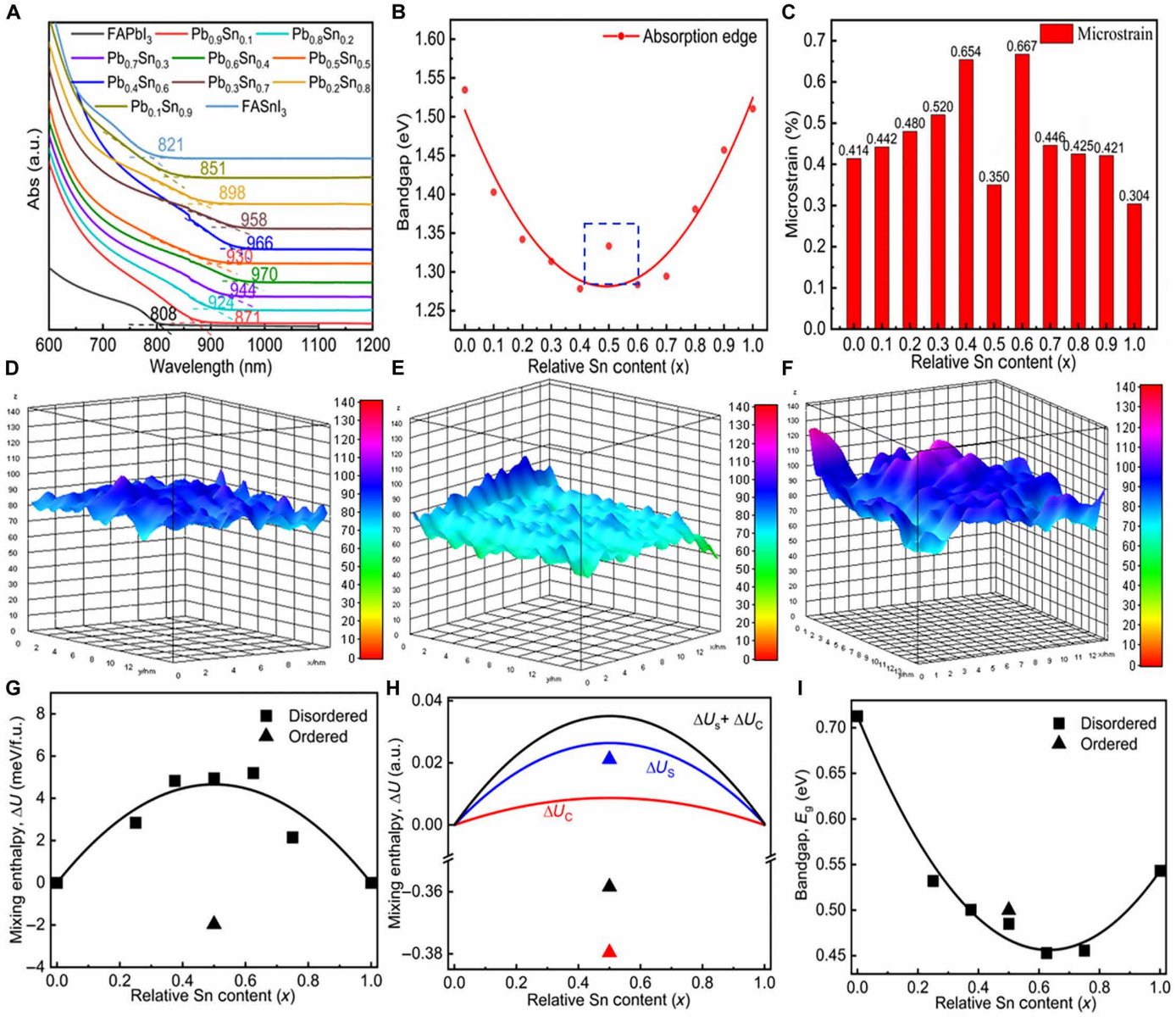

Fig. 4. Investigation of the physical mechanism behind the bandgap bowing effect of $FAPb_{1-x}Sn_xI_3$ TLP nanocrystals. (**A**) UV-visible absorption spectra of TLP nanocrystals with various *x*. (**B**) Bandgaps derived from the spectra of (A), along with the simulated bowing curves dependent on the relative Sn content (*x*). (**C**) Microstrain values derived from their corresponding XRD patterns. (**D** to **F**) Two-dimensional intensity profiles of atomic lattices of three typical TLP nanocrystals with Pb/Sn ratios of 6:4, 5:5, and 4:6. (**G**) Calculated mixing enthalpies of $FAPb_{1-x}Sn_xI_3$ alloy at different Sn concentrations $x = 0.0, 0.25, 0.375, 0.50, 0.625, 0.75$, and 1.0. The solid lines are fitted by calculated results (squares) of special quasirandom structures at different compositions, with interaction parameter $\Omega = 18.65$ meV. The results of the stable ordered structures at $x = 0.5$ are shown as triangles. (**H**) Model for describing the mixing enthalpies at different compositions, where the total effects of strain energy (ΔU_S) and Coulomb energy (ΔU_C) lead to the lowest energy at $x = 0.5$ for the ordered compound. The fitted points for disordered alloy are not shown for clarity. (**I**) Calculated bandgaps of $FAPb_{1-x}Sn_xI_3$ alloy at different Sn concentrations for both the disordered and ordered alloys.

mixing enthalpy becomes negative and obviously lower than that of other compositions. This behavior is typical for ionic alloys with predominantly Coulomb interactions and coincides with the experimental observations as indicated by the intensity profiles of atomic lattices discussed above (Fig. 4, D to F). Replacing the Cs cation with formamidinium, the calculated mixing enthalpies ΔU of $FAPb_{1-x}Sn_xI_3$ with compositions at $x = 0.0, 0.25, 0.375, 0.50, 0.625, 0.75$, and 1.0 are shown in Fig. 4G. The critical temperature (T_C) of $FAPb_{1-x}Sn_xI_3$ is then calculated to be 112 K, which means that the $FAPb_{1-x}Sn_xI_3$ alloy is thermodynamically stable at room temperature (300 K). As expected, the negative mixing enthalpy of $FAPb_{0.5}Sn_{0.5}I_3$ indicates the formation of an ordered structure of the alloy at $x = 0.5$ (fig. S13B).

To deepen our understanding of the energetics of $FAPb_{1-x}Sn_xI_3$ alloy, we construct a physical model that includes the effects of the strain and Coulomb interactions for both the disordered and ordered $FAPb_{1-x}Sn_xI_3$ alloys; see Fig. 4H. The strain energy in disordered

$FAPb_{1-x}Sn_xI_3$ alloys is always positive, indicating an increase in energy because of strain caused by the atomic size mismatch between Sn and Pb. With the perfect ordering of Pb-Sn at $x = 0.5$, where alternate Sn and Pb occupy the simple cubic sublattice, the positive strain energy is minimized. That is consistent with the changes of the measured microstrains discussed in Fig. 4C. Moreover, for the ordered $FAPb_{1-x}Sn_xI_3$ alloy at $x = 0.5$, the magnitude of the negative Coulomb energy is maximized, leading to an energy gain in mixing enthalpy. This energy gain is attributed to the charge redistribution in ionic alloys (*41*). With the disorder-order phase transition and its corresponding strain reduction, the calculated bandgaps of $FAPb_{1-x}Sn_xI_3$ alloys at various compositions are shown in Fig. 4I. The bandgap of $FAPb_{0.5}Sn_{0.5}I_3$ in the ordered configuration shows the same jumping over the bowing curve as observed in the experiment discussed in Fig. 4B. That larger bandgap of $FAPb_{0.5}Sn_{0.5}I_3$ can be ascribed to a stronger coupling between unoccupied conduction bands and occupied valence bands.

Optoelectronic devices of concept with an emission wavelength over 900 nm

To demonstrate the application of our infrared TLP nanocrystals, we fabricated LEDs on the basis of three kinds of TLP nanocrystals with the reddest PL emission, including $FAPb_{0.6}Sn_{0.4}I_3$, $FAPb_{0.5}Sn_{0.5}I_3$, and $FAPb_{0.4}Sn_{0.6}I_3$. The device configuration of indium tin oxide (ITO)/poly(3,4-ethylenedioxythiophene):poly(styrene sulfonate) (PEDOT:PSS)/poly(*N*-vinylcarbazole) (P-NV)/TLP/2,2′,2″-(1,3,5-benzinetriyl)-tris(1-phenyl-1*H*-benzimidazole) (TBPi)/Al is illustrated in fig. S14. The electronic structures of the three TLP nanocrystals were defined by ultraviolet (UV) photoelectron spectroscopy (UPS) with the cutoff and onset values shown in fig. S15. The Fermi levels (E_F) of the three TLP nanocrystals were determined at −3.59, −3.58, and −3.39 eV for the above three TLP nanocrystal films, respectively. Derived from the tails shown in fig. S9, their valence band maxima are determined at −4.57, −4.37, and −4.25 eV, respectively, which agree well with the p-orbital uplift trend of valence band maximum by substituting Pb with Sn when increasing the Sn content. The band-level structures of their LED devices are also illustrated in Fig. 5A.

Electroluminescence (EL) emission peaks for $FAPb_{0.6}Sn_{0.4}I_3$, $FAPb_{0.5}Sn_{0.5}I_3$, and $FAPb_{0.4}Sn_{0.6}I_3$ are 919, 915, and 930 nm (Fig. 5B), respectively. Compared with their corresponding PL ones, the blue shift of emission peaks may be attributed to the generation of Joule heating by nonradiative Auger recombination. For the PL process, the hot Auger electron generated by exciton recombination could thermally dissipate its energy at a very fast rate inside the same material instead of being injected across the interface into the light-emitting material (*45*). The optical image of the $FAPb_{0.4}Sn_{0.6}I_3$-based demo device was recorded by an infrared camera (Fig. 5C) with the corresponding general photo inserted. The perovskite LED presents a central emission wavelength of 930 nm and a full width at half maximum of 86 nm. Meanwhile, the optimized LED presents an external quantum efficiency (EQE) of 0.034% at 10.6 V. Although the demo device shows low EQE, the infrared-emission optoelectronic devices based on our $FAPb_{1-x}Sn_xI_3$ TLP nanocrystals were successfully realized with an emission wavelength over 900 nm.

DISCUSSION

First, we successfully synthesized fully stoichiometric $FAPb_{1-x}Sn_xI_3$ TLP monocrystalline nanocrystals by the hot-injection solution method. The Sn:Pb stoichiometric ratio of each kind of TLP nanocrystal was determined by ICP-MS, which was realized by tuning the input ratio of SnI_2/PbI_2. For example, that input ratio was set to 100:1 to get $FAPb_{0.1}Sn_{0.9}I_3$ nanocrystals because the soluble Sn-TOP complex in the reaction solution does not easily release Sn to form TLP nanocrystals compared with Pb-containing intermediates. Those TLP nanocrystals have a narrow size distribution at an average size of 15 nm, relying on the effect of used long-chain ligands, especially OLA and TOP.

Second, atomic-level lattice images of $FAPb_{1-x}Sn_xI_3$ TLP monocrystalline nanocrystals were clearly recorded by cryo-TEM. Because of easy delocalization of $5s^2$ electrons, the recording of the atomic-level lattice of Sn-based perovskites is much more difficult and has never been reported before. Cryo-TEM is a more suitable protocol to record the atomic-level lattice of perovskites, which offers the cryogenic environment with liquid nitrogen and can control precisely the EB dose. That suppresses the $5s^2$ electron loss of Sn^{2+}, allowing to capture the atomic-level lattice images. Besides, the long-chain capping ligands are examined to preserve the stability of the nanocrystal lattice and enable the successful atomic-level recording.

Third, depending on fully stoichiometric $FAPb_{1-x}Sn_xI_3$ TLP monocrystalline nanocrystals synthesized, we plotted an intact Sn:Pb ratio–dependent bandgap-varying diagram. That allows us to get a full scope view of its bandgap bowing behavior on a platform of monocrystalline

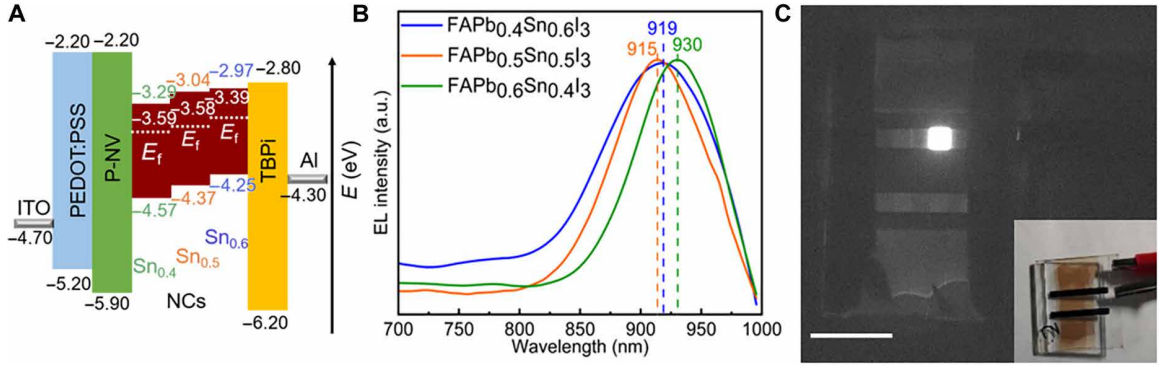

Fig. 5. Optoelectronic devices of concept based on $FAPb_{0.6}Sn_{0.4}I_3$, $FAPb_{0.5}Sn_{0.5}I_3$, and $FAPb_{0.4}Sn_{0.6}I_3$ nanocrystals. (**A**) Energy-level diagram of the three LED devices. NCs, nanocrystals. (**B**) EL spectra of the LEDs based on $FAPb_{1-x}Sn_xI_3$ nanocrystals ($x = 0.4$, 0.5, and 0.6). (**C**) Photographs of hybrid perovskite LED taken with an infrared camera. The inset is the corresponding photograph taken with a common camera at a scale bar of 1 cm.

nanocrystals with the lattice strains preserved well other than polycrystalline films with the strains relaxed. As we know, the polycrystalline TLP films suffer severely from inevitable composition and phase segregations. Critically, disorder-order phase transition induced by strain and Coulomb interactions is revealed for $FAPb_{1-x}Sn_xI_3$ near $x = 0.5$, which disrupts the gradual bandgap bowing of $FAPb_{1-x}Sn_xI_3$. That puzzling bandgap variation behavior found in this system has never been discussed before. Our discovery completes the critical piece of jigsaw of TLP materials and would also contribute to the understanding and future designs of Sn-Pb alloyed metal-halide perovskite materials.

Last, we built the demo LED devices on the basis of the three TLP nanocrystals with the PL emission wavelength over 900 nm. As expected, these three LEDs emitted infrared lights with the wavelength as far as 930 nm. Nevertheless, the presence of long-chain ligands capping on nanocrystals would impede carriers' transport and limits the optoelectronic performance of those LEDs. By using appropriate short-chain ligands to replace the original long-chain ones, it would improve the device performance further. In view of this point, our work affords a promising material candidate to bridge the critical gap around 900 nm in the commercial market of both light sources and photodetectors.

MATERIALS AND METHODS

Materials

Formamidine acetate (Energy Chemical, 99%), SnI_2 (3A, 99.999%), PbI_2 (TCI, 99.99%), octadecene (Aladdin, 90%), OAc (Energy Chemical, 90%), OLA (Energy Chemical, 90%), TOP (Aladdin, 90%), toluene (Yonghua Chemical, extra dry 99.5%), and hexane (Energy Chemical, extra dry 97%) were used in this study. PEDOT:PSS (Clevios AI 4083), P-NV, and TBPi were purchased from Luminescence Technology Corp.

Synthesis of TLP nanocrystals

Colloidal mixed $FAPb_{1-x}Sn_xI_3$ nanocrystals were synthesized by a modified hot-injection method. Different mole ratios of SnI_2 and PbI_2 were mixed with TOP (2 ml), OAc (1 ml), and ODE (8 ml) in a 40-ml glass bottle, then the mixture was vigorously stirred overnight at room temperature in N_2, and after stirring overnight, the mixture was heated to 80°C for about 3 hours, followed by the addition of OLA (60 μl) to prepare the hybrid Pb-Sn precursor solution. Formamidine acetate (0.208 g), ODE (3 ml), and OAc (2 ml) were mixed in a 20-ml vial on a hot plate and heated at 120°C until all of formamidine acetate reacted with OAc to form a yellow clear formamidine oleate precursor solution. $FAPb_{1-x}Sn_xI_3$ nanocrystals were synthesized by swiftly injecting the formamidine oleate precursor (1 ml) into the hybrid Pb-Sn precursor solution under vigorous stirring in N_2. After cooling to room temperature, the solution was centrifuged at 10,000 rpm for 5 min to remove aggregated nanocrystals, the supernatant was discarded, and the precipitate was redispersed in toluene (10 ml); the solution was also centrifuged at 10,000 rpm for 5 min to purify the nanocrystals, and then the supernatant was discarded and the precipitate was redispersed in hexene as fresh samples for other experiments.

Characterizations

X-ray diffraction

The phase analysis of a series of colloidal $FAPb_{1-x}Sn_xI_3$ nanocrystals was performed by XRD analyses (Rigaku Smartlab, 9 kW) with Cu Kα ($\lambda = 1.54$ Å) radiation. The spectra were collected with an angular range of $10° < 2\theta < 90°$ following a 0.01° step. The XRD analyses were performed at room temperature (298 K) and the sample temperature that is a lower testing temperature (after dropping in liquid nitrogen and quickly moving to an XRD testing holder) to explore the crystal structure of $FAPb_{1-x}Sn_xI_3$ perovskite nanocrystals at room temperature and the temperature after dealing with a similar process with cryo-TEM measurements.

Inductively coupled plasma mass spectrometry

The content of Pb and Sn in a series of $FAPb_{1-x}Sn_xI_3$ nanocrystals was measured by ICP-MS with an Agilent Technologies 7700 Series ICP-MS. Samples were prepared as follows: A portion of the solvent (hexane) was nitrified with nitric acid for about 2 hours to form a clear transparent solvent, which was diluted with pure water to prepare the sample for ICP-MS measurements.

UV and PL

The absorption spectra were taken using a Shimadzu UV-visible spectrophotometer (UV-3600) with cuvettes. Room-temperature PL spectra were measured by Edinburgh instruments FLS1000 with cuvettes too.

^{1}H NMR and FTIR

^{1}H NMR spectra were collected on a Bruker Avance 500 spectrometer in deuterated chloroform. FTIR spectra were characterized by a Bruker Vertex 70v. A portion of the solvent (hexane) was evaporated to obtain a solid sample for FTIR measurements.

XPS and UPS

XPS measurements were carried out on an Omicron ESCA Probe XPS spectrometer (ESCALAB 250Xi, Thermo Fisher Scientific) using 150-eV pass energy and 1-eV step size for the survey scan and 20-eV pass energy and 0.01-eV step size for the fine scan. The XPS spectra were calibrated by the binding energy of 284.8 eV for C 1s. To measure the work function, UPS spectra were recorded with an Imaging Photoelectron Spectrometer (Axis Ultra, Kratos Analytical Ltd.), with a nonmonochromated He Iα photon source ($h\nu = 21.22$ eV). Au is used as a reference.

TEM tests

Cryo-TEM

For TLP nanocrystals, owing to their moisture/oxygen and EB sensitivity, we developed the cryo-TEM sample preparation method. The Sn-Pb nanocrystals were dropped into a carbon-coated TEM Cu grid and annealed at 60°C for 10 min in a N_2-filled glove box. The TEM Cu grid was immediately loaded to a cryogenic chamber of Titan Krios cryo-TEM (Thermo Fisher Scientific). In conventional high-resolution TEM, Sn-Pb nanocrystals will be damaged in several seconds under the dose rate of 50 e $Å^{-2}$ s^{-1}. In contrast, the cryo–transmission electron microscope equipped with a direct electron camera (Falcon IV, Thermo Fisher Scientific) could precisely control the electron dose rate to alleviate the damage during the imaging process. To minimize the electron damage for Sn-Pb nanocrystals, the electron dose rates for high-magnification (120k×) and low-magnification cryo-TEM images were adjusted to be 25 and 1.5 e $Å^{-2}$ s^{-1}, respectively.

Double Cs–corrected STEM and EDS

Scanning TEM (STEM) and energy-dispersive x-ray spectroscopy (EDS) specimen preparation was similar to the method mentioned above. Before the TEM Cu grid was inserted into a double Cs–corrected transmission electron microscope (Titan Themis 300 kV), the sample loaded into an FEI double tilt holder was cleaned for 2 s

with plasma (mixture of 95% Ar and 5% oxygen). The STEM images were acquired at 0.05 nA (screen current).

LED demo device fabrication and tests

First, the ITO-coated glass substrates with a sheet resistance of 25 ohms per square were rinsed in ultrasonic detergent and deionized water for 30 min in sequence and then dried in an oven at 60°C for 30 min. Before the deposition of functional layers, the ITO-coated glass substrates were treated by a UV-ozone cleaner for 30 min. After treatment, PEDOT:PSS (Clevios AI 4083) was spun cast at 3000 rpm for 45 s and baked at 130°C for 20 min in air. Then, the samples were transferred to a N_2-filled glove box to sequentially fabricate the following layers. The P-NV solution (8 mg ml^{-1} in chlorobenzene) was spun cast at 3000 rpm for 45 s and baked at 120°C for 20 min. The nanocrystals (50 mg ml^{-1} in octane solution) were spun cast on the top of P-NV at 3000 rpm for 45 s, followed by baking at 100°C for 5 min. Last, the samples were transferred to a vacuum evaporator (base pressure, 5×10^{-4} Pa) for TBPi layer and Al cathode deposition. The EL spectra of quantum dot LEDs were measured simultaneously by a commercialized system (Guangzhou XiPu Optoelectronics Technology Co., Ltd.) that was equipped with a fiber-optic spectrometer (XPFS1000-TEC) and a photodetector array (S7031-1006, Hamamatsu Photonics).

Supplementary Materials

This PDF file includes:

Supplementary Text
Figs. S1 to S15
Tables S1 and S2
References

REFERENCES AND NOTES

1. F. Hao, C. C. Stoumpos, R. P. H. Chang, M. G. Kanatzidis, Anomalous band gap behavior in mixed Sn and Pb perovskites enables broadening of absorption spectrum in solar cells. *J. Am. Chem. Soc.* **136**, 8094–8099 (2014).
2. C. Wang, Z. Song, C. Li, D. Zhao, Y. Yan, Low-bandgap mixed tin-lead perovskites and their applications in all-perovskite tandem solar cells. *Adv. Funct. Mater.* **29**, 1808801 (2019).
3. J. Tong, Z. Song, D. H. Kim, X. Chen, C. Chen, A. F. Palmstrom, P. F. Ndione, M. O. Reese, S. P. Dunfield, O. G. Reid, J. Liu, F. Zhang, S. P. Harvey, Z. Li, S. T. Christensen, G. Teeter, D. Zhao, M. M. Al-Jassim, M. F. A. M. van Hest, M. C. Beard, S. E. Shaheen, J. J. Berry, Y. Yan, K. Zhu, Carrier lifetimes of >1 μs in Sn-Pb perovskites enable efficient all-perovskite tandem solar cells. *Science* **364**, 475–479 (2019).
4. J. Zhu, Y. Xu, Y. Luo, J. Luo, R. He, C. Wang, Y. Wang, K. Wei, Z. Yi, Z. Gao, J. Wang, J. You, Z. Zhang, H. Lai, S. Ren, X. Liu, C. Xiao, C. Chen, J. Zhang, F. Fu, D. Zhao, Custom-tailored hole transport layer using oxalic acid for high-quality tin-lead perovskites and efficient all-perovskite tandems. *Sci. Adv.* **10**, eadl2063 (2024).
5. W.-H. Gao, C. Chen, Perovskites and their constructed near-infrared photodetectors. *Nano Energy* **128**, 109904 (2024).
6. H. Yu, W. Chen, Z. Fang, L. Ding, B. Cao, Z. Xiao, Alkalis-doping of mixed tin-Lead perovskites for efficient near-infrared light-emitting diodes. *Sci. Bull.* **67**, 54–60 (2022).
7. J. Yang, Mapping temperature-dependent energy–structure–property relationships for solid solutions of inorganic halide perovskites. *J. Mater. Chem. C* **8**, 16815–16825 (2020).
8. E. S. Parrott, T. Green, R. L. Milot, M. B. Johnston, H. J. Snaith, L. M. Herz, Interplay of structural and optoelectronic properties in formamidinium mixed tin–lead triiodide perovskites. *Adv. Funct. Mater.* **28**, 1802803 (2018).
9. K. J. Savill, A. M. Ulatowski, L. M. Herz, Optoelectronic properties of tin–lead halide perovskites. *ACS Energy Lett.* **6**, 2413–2426 (2021).
10. A. Mehta, J. Im, B. H. Kim, H. Min, R. Nie, S. I. Seok, Stabilization of lead–tin-alloyed inorganic-organic halide perovskite quantum dots. *ACS Nano* **12**, 12129–12139 (2018).
11. X. Wu, X. Ke, M. Sui, Recent progress on advanced transmission electron microscopy characterization for halide perovskite semiconductors. *J. Semicond.* **43**, 041106 (2022).
12. D. Zhang, Y. Zhu, L. Liu, X. Ying, C.-E. Hsiung, R. Sougrat, K. Li, Y. Han, Atomic-resolution transmission electron microscopy of electron beam–sensitive crystalline materials. *Science* **359**, 675–679 (2018).
13. Y. Li, W. Zhou, Y. Li, W. Huang, Z. Zhang, G. Chen, H. Wang, G.-H. Wu, N. Rolston, R. Vila, W. Chiu, Y. Cui, Unravelling atomic structure and degradation mechanisms of organic-inorganic halide perovskites by cryo-EM. *Joule* **3**, 2854–2866 (2019).
14. M. U. Rothmann, J. S. Kim, J. Borchert, K. B. Lohmann, C. M. O'Leary, A. A. Sheader, L. Clark, H. J. Snaith, M. B. Johnston, P. D. Nellist, L. M. Herz, Atomic-scale microstructure of metal halide perovskite. *Science* **370**, eabb5940 (2020).
15. D. Han, J. Wang, L. Agosta, Z. Zang, B. Zhao, L. Kong, H. Lu, I. Mosquera-Lois, V. Carnevali, J. Dong, J. Zhou, H. Ji, L. Pfeifer, S. M. Zakeeruddin, Y. Yang, B. Wu, U. Rothlisberger, X. Yang, M. Grätzel, N. Wang, Tautomeric mixture coordination enables efficient lead-free perovskite LEDs. *Nature* **622**, 493–498 (2023).
16. G. M. Dalpian, X.-G. Zhao, L. Kazmerski, A. Zunger, Formation and composition-dependent properties of alloys of cubic halide perovskites. *Chem. Mater.* **31**, 2497–2506 (2019).
17. W. Liao, D. Zhao, Y. Yu, N. Shrestha, K. Ghimire, C. R. Grice, C. Wang, Y. Xiao, A. J. Cimaroli, R. J. Ellingson, N. J. Podraza, K. Zhu, R.-G. Xiong, Y. Yan, Fabrication of efficient low-bandgap perovskite solar cells by combining formamidinium tin iodide with methylammonium lead iodide. *J. Am. Chem. Soc.* **138**, 12360–12363 (2016).
18. W. Zhang, H. Yuan, X. Li, X. Guo, C. Lu, A. Liu, H. Yang, L. Xu, X. Shi, Z. Fang, H. Yang, Y. Cheng, J. Fang, Component distribution regulation in Sn-Pb perovskite solar cells through selective molecular interaction. *Adv. Mater.* **35**, e2303674 (2023).
19. A. F. Gualdrón-Reyes, S. J. Yoon, E. M. Barea, S. Agouram, V. Muñoz-Sanjosé, Á. M. Meléndez, M. E. Niño-Gómez, I. Mora-Seró, Controlling the phase segregation in mixed halide perovskites through nanocrystal size. *ACS Energy Lett.* **4**, 54–62 (2019).
20. F. Liu, C. Ding, Y. Zhang, T. S. Ripolles, T. Kamisaka, T. Toyoda, S. Hayase, T. Minemoto, K. Yoshino, S. Dai, M. Yanagida, H. Noguchi, Q. Shen, Colloidal synthesis of air-stable alloyed $CsSn_{1-x}Pb_xI_3$ perovskite nanocrystals for use in solar cells. *J. Am. Chem. Soc.* **139**, 16708–16719 (2017).
21. Y. Chen, J. Yin, Q. Wei, C. Wang, X. Wang, H. Ren, S. F. Yu, O. M. Bakr, O. F. Mohammed, M. Li, Multiple exciton generation in tin–lead halide perovskite nanocrystals for photocurrent quantum efficiency enhancement. *Nat. Photon.* **16**, 485–490 (2022).
22. A. Rajagopal, R. J. Stoddard, H. W. Hillhouse, A. K.-Y. Jen, On understanding bandgap bowing and optoelectronic quality in Pb–Sn alloy hybrid perovskites. *J. Mater. Chem. A* **7**, 16285–16293 (2019).
23. A. Goyal, S. McKechnie, D. Pashov, W. Tumas, M. van Schilfgaarde, V. Stevanović, Origin of pronounced nonlinear band gap behavior in lead–tin hybrid perovskite alloys. *Chem. Mater.* **30**, 3920–3928 (2018).
24. G. E. Eperon, T. Leijtens, K. A. Bush, R. Prasanna, T. Green, J. T.-W. Wang, D. P. McMeekin, G. Volonakis, R. L. Milot, R. May, A. Palmstrom, D. J. Slotcavage, R. A. Belisle, J. B. Patel, E. S. Parrott, R. J. Sutton, W. Ma, F. Moghadam, B. Conings, A. Babayigit, H.-G. Boyen, S. Bent, F. Giustino, L. M. Herz, M. B. Johnston, M. D. McGehee, H. J. Snaith, Perovskite-perovskite tandem photovoltaics with optimized band gaps. *Science* **354**, 861–865 (2016).
25. S. Kahmann, Z. Chen, O. Hordiichuk, O. Nazarenko, S. Shao, M. V. Kovalenko, G. R. Blake, S. Tao, M. A. Loi, Compositional variation in $FAPb_{1-x}Sn_xI_3$ and its impact on the electronic structure: A combined density functional theory and experimental study. *ACS Appl. Mater. Interfaces* **14**, 34253–34261 (2022).
26. F. Valadares, I. Guilhon, L. K. Teles, M. Marques, Atomistic origins of enhanced band gap, miscibility, and oxidation resistance in α-$CsPb_{1-x}Sn_xI_3$ mixed perovskite. *J. Phys. Chem. C* **124**, 26124–26133 (2020).
27. L. Dai, Z. Deng, F. Auras, H. Goodwin, Z. Zhang, J. C. Walmsley, P. D. Bristowe, F. Deschler, N. C. Greenham, Slow carrier relaxation in tin-based perovskite nanocrystals. *Nat. Photon.* **15**, 696–702 (2021).
28. S. Mourdikoudis, M. Menelaou, N. Fiuza-Maneiro, G. Zheng, S. Wei, J. Pérez-Juste, L. Polavarapu, Z. Sofer, Oleic acid/oleylamine ligand pair: A versatile combination in the synthesis of colloidal nanoparticles. *Nanoscale Horiz.* **7**, 941–1015 (2022).
29. H. Chen, A. Maxwell, C. Li, S. Teale, B. Chen, T. Zhu, E. Ugur, G. Harrison, L. Grater, J. Wang, Z. Wang, L. Zeng, S. M. Park, L. Chen, P. Serles, R. A. Awni, B. Subedi, X. Zheng, C. Xiao, N. J. Podraza, T. Filleter, C. Liu, Y. Yang, J. M. Luther, S. De Wolf, M. G. Kanatzidis, Y. Yan, E. H. Sargent, Regulating surface potential maximizes voltage in all-perovskite tandems. *Nature* **613**, 676–681 (2023).
30. B.-B. Zhang, J.-K. Chen, C. Zhang, N. Shirahata, H.-T. Sun, Mechanistic insight into the precursor chemistry of cesium tin iodide perovskite nanocrystals. *ACS Materials Lett.* **5**, 1954–1961 (2023).
31. D. H. Fabini, C. C. Stoumpos, G. Laurita, A. Kaltzoglou, A. G. Kontos, P. Falaras, M. G. Kanatzidis, R. Seshadri, Reentrant structural and optical properties and large positive thermal expansion in perovskite formamidinium lead iodide. *Angew. Chem. Int. Ed.* **55**, 15392–15396 (2016).
32. D. B. Mitzi, K. Liang, Synthesis, resistivity, and thermal properties of the cubic perovskite $NH_2CH{=}NH_2SnI_3$ and related systems. *J. Solid State Chem.* **134**, 376–381 (1997).
33. Z. Zhang, X. Tian, C. Wang, J. Jin, Y. Jiang, Q. Zhou, J. Zhu, J. Xu, R. He, Y. Huang, S. Ren, C. Chen, P. Gao, R. Long, D. Zhao, Revealing superoxide-induced degradation in lead-free tin perovskite solar cells. *Energ. Environ. Sci.* **15**, 5274–5283 (2022).

34. C.-Q. Yang, R. Zhi, M. U. Rothmann, Y.-Y. Xu, L.-Q. Li, Z.-Y. Hu, S. Pang, Y.-B. Cheng, G. Van Tendeloo, W. Li, Unveiling the intrinsic structure and intragrain defects of organic–inorganic hybrid perovskites by ultralow dose transmission electron microscopy. *Adv. Mater.* **35**, e2211207 (2023).
35. W. Chen, B. Han, Q. Hu, M. Gu, Y. Zhu, W. Yang, Y. Zhou, D. Luo, F.-Z. Liu, R. Cheng, R. Zhu, S.-P. Feng, A. B. Djurišić, T. P. Russell, Z. He, Interfacial stabilization for inverted perovskite solar cells with long-term stability. *Sci. Bull.* **66**, 991–1002 (2021).
36. M. Li, R. Begum, J. Fu, Q. Xu, T. M. Koh, S. A. Veldhuis, M. Grätzel, N. Mathews, S. Mhaisalkar, T. C. Sum, Low threshold and efficient multiple exciton generation in halide perovskite nanocrystals. *Nat. Commun.* **9**, 4197 (2018).
37. D. N. Dirin, A. Vivani, M. Zacharias, T. V. Sekh, I. Cherniukh, S. Yakunin, F. Bertolotti, M. Aebli, R. D. Schaller, A. Wieczorek, S. Siol, C. Cancellieri, L. P. H. Jeurgens, N. Masciocchi, A. Guagliardi, L. Pedesseau, J. Even, M. V. Kovalenko, M. I. Bodnarchuk, Intrinsic formamidinium tin iodide nanocrystals by suppressing the Sn(IV) impurities. *Nano Lett.* **23**, 1914–1923 (2023).
38. J. Jeong, M. Kim, J. Seo, H. Lu, P. Ahlawat, A. Mishra, Y. Yang, M. A. Hope, F. T. Eickemeyer, M. Kim, Y. J. Yoon, I. W. Choi, B. P. Darwich, S. J. Choi, Y. Jo, J. H. Lee, B. Walker, S. M. Zakeeruddin, L. Emsley, U. Rothlisberger, A. Hagfeldt, D. S. Kim, M. Grätzel, J. Y. Kim, Pseudo-halide anion engineering for α-$FAPbI_3$ perovskite solar cells. *Nature* **592**, 381–385 (2021).
39. B.-B. Yu, Z. Chen, Y. Zhu, Y. Wang, B. Han, G. Chen, X. Zhang, Z. Du, Z. He, Heterogeneous 2D/3D tin-halides perovskite solar cells with certified conversion efficiency breaking 14%. *Adv. Mater.* **33**, e2102055 (2021).
40. J. Im, C. C. Stoumpos, H. Jin, A. J. Freeman, M. G. Kanatzidis, Antagonism between spin–orbit coupling and steric effects causes anomalous band gap evolution in the perovskite photovoltaic materials $CH_3NH_3Sn_{1-x}Pb_xI_3$. *J. Phys. Chem. Lett.* **6**, 3503–3509 (2015).
41. Q. Gao, H. Sahin, J. Kang, S.-H. Wei, Origin of anomalous band-gap bowing in two-dimensional tin-lead mixed perovskite alloys. *Phys. Rev. B* **104**, 064204 (2021).
42. A. Rajagopal, R. J. Stoddard, S. B. Jo, H. W. Hillhouse, A. K.-Y. Jen, Overcoming the photovoltage plateau in large bandgap perovskite photovoltaics. *Nano Lett.* **18**, 3985–3993 (2018).
43. D. Liu, D. Luo, A. N. Iqbal, K. W. P. Orr, T. A. S. Doherty, Z.-H. Lu, S. D. Stranks, W. Zhang, Strain analysis and engineering in halide perovskite photovoltaics. *Nat. Mater.* **20**, 1337–1346 (2021).
44. I. Lazić, E. G. T. Bosch, in *Advances in Imaging and Electron Physics*, P. W. Hawkes, Ed. (Elsevier, 2017), vol. 199, pp. 75–184.
45. W. K. Bae, Y.-S. Park, J. Lim, D. Lee, L. A. Padilha, H. McDaniel, I. Robel, C. Lee, J. M. Pietryga, V. I. Klimov, Controlling the influence of Auger recombination on the performance of quantum-dot light-emitting diodes. *Nat. Commun.* **4**, 2661 (2013).
46. A. Pramanick, X. P. Wang, C. Hoffmann, S. O. Diallo, M. R. V. Jørgensen, X.-L. Wang, Microdomain dynamics in single-crystal $BaTiO_3$ during paraelectric-ferroelectric phase transition measured with time-of-flight neutron scattering. *Phys. Rev. B* **92**, 174103 (2015).
47. F. Zaza, G. Orio, E. Serra, F. Caprioli, M. Pasquali, Low-temperature capacitive sensor based on perovskite oxides. *AIP Conf. Proc.* **1667**, 020004 (2015).
48. P. Scherrer, Bestimmung der größe und der inneren struktur von kolloidteilchen mittels röntgenstrahlen. *Nachr. Ges. Wiss. Goettingen Math. Phys. Kl.* **1918**, 98–100 (1918). [Determination of the size and internal structure of colloid particles using x-rays]
49. K. Nishimura, D. Hirotani, M. A. Kamarudin, Q. Shen, T. Toyoda, S. Iikubo, T. Minemoto, K. Yoshino, S. Hayase, Relationship between lattice strain and efficiency for sn-perovskite solar cells. *ACS Appl. Mater. Interfaces* **11**, 31105–31110 (2019).
50. A. R. Stokes, A. J. C. Wilson, The diffraction of X rays by distorted crystal aggregates - I. *Proc. Phys. Soc.* **56**, 174–181 (1944).
51. G. K. Williamson, W. H. Hall, X-ray line broadening from filed aluminium and wolfram. *Acta Metall.* **1**, 22–31 (1953).
52. N. J. Jeon, J. H. Noh, W. S. Yang, Y. C. Kim, S. Ryu, J. Seo, S. I. Seok, Compositional engineering of perovskite materials for high-performance solar cells. *Nature* **517**, 476–480 (2015).
53. Z. Li, M. Yang, J.-S. Park, S.-H. Wei, J. J. Berry, K. Zhu, Stabilizing perovskite structures by tuning tolerance factor: Formation of formamidinium and cesium lead iodide solid-state alloys. *Chem. Mater.* **28**, 284–292 (2015).
54. Y. Yu, C. Wang, C. R. Grice, N. Shrestha, J. Chen, D. Zhao, W. Liao, A. J. Cimaroli, P. J. Roland, R. J. Ellingson, Y. Yan, Improving the performance of formamidinium and cesium lead triiodide perovskite solar cells using lead thiocyanate additives. *ChemSusChem* **9**, 3288–3297 (2016).
55. J. Liu, G. Wang, Z. Song, X. He, K. Luo, Q. Ye, C. Liao, J. Mei, $FAPb_{1-x}Sn_xI_3$ mixed metal halide perovskites with improved light harvesting and stability for efficient planar heterojunction solar cells. *J. Mater. Chem. A* **5**, 9097–9106 (2017).
56. G. Kresse, J. Furthmüller, Efficient iterative schemes for ab initio total-energy calculations using a plane-wave basis set. *Phys. Rev. B* **54**, 11169–11186 (1996).
57. J. P. Perdew, K. Burke, M. Ernzerhof, Generalized gradient approximation made simple. *Phys. Rev. Lett.* **77**, 3865–3868 (1996).
58. S. Grimme, J. Antony, S. Ehrlich, H. Krieg, A consistent and accurate ab initio parametrization of density functional dispersion correction (DFT-D) for the 94 elements H-Pu. *J. Chem. Phys.* **132**, 154104 (2010).
59. R. Gao, J. Kang, Unusual band gap bowing in $CsCd_xPb_{(1-x)}Br_3$ alloys due to a chemical mismatch. *J. Phys. Chem. Lett.* **14**, 10670–10676 (2023).
60. A. Zunger, S.-H. Wei, L. G. Ferreira, J. E. Bernard, Special quasirandom structures. *Phys. Rev. Lett.* **65**, 353–356 (1990).
61. S.-H. Wei, L. G. Ferreira, J. E. Bernard, A. Zunger, Electronic properties of random alloys: Special quasirandom structures. *Phys. Rev. B* **42**, 9622–9649 (1990).
62. A. van de Walle, M. Asta, G. Ceder, The alloy theoretic automated toolkit: A user guide. *Calphad* **26**, 539–553 (2002).
63. R. M. Martin, Elastic properties of ZnS structure semiconductors. *Phys. Rev. B* **1**, 4005–4011 (1970).
64. R. Magri, S.-H. Wei, A. Zunger, Ground-state structures and the random-state energy of the Madelung lattice. *Phys. Rev. B* **42**, 11388–11391 (1990).
65. W.-J. Yin, Y. Yan, S.-H. Wei, Anomalous alloy properties in mixed halide perovskites. *J. Phys. Chem. Lett.* **5**, 3625–3631 (2014).

Acknowledgments: We thank the Department of Materials Science and Engineering in SUSTech for the characterizations in this work and computational resources from the Beijing Computational Science Research Center. **Funding:** This work was supported by the National Natural Science Foundation of China (NSFC) (nos. 52273266 and U2001216), the Shenzhen Key Laboratory Project (no. ZDSYS201602261933302), Shenzhen Science and Technology Innovation Committee (nos. 20231121102401001; JCYJ20200109141412308), Guangdong-Hongkong-Macau Joint Laboratory on Micro-Nano Manufacturing Technology (no. 2021LSYS004), and SUSTech high-level special funds (G03050K002). S.-H.W. and Z.C. appreciate the funding from the National Natural Science Foundation of China (nos. 12088101, 11991060, and U2230402) and the China Postdoctoral Science Foundation (nos. 2023M730197 and GZB20230052). **Author contributions:** Z.H. conceived the idea and supervised the project. H.G. synthesized all $FAPb_{1-x}Sn_xI_3$ TLP nanocrystals and conducted XRD, ICP-MS, UV, and PL characterizations. Dong He and H.G. performed cryo-TEM characterizations. Z.C. carried out the calculations and discussed the data. P.G. fabricated the LED demo device and performed EL characterizations under the direction of S.C. Dong He and Dongsheng He carried out double Cs–corrected STEM and EDS characterizations. Z.L. performed ^{1}H NMR spectral characterizations. Q.S. conducted XPS and UPS characterizations. X.Z. performed the FTIR characterizations. J.X. was involved in the analysis of cryo-TEM results. Z.H. and H.G. analyzed all data and wrote the paper. S.-H.W. and S.-H.Y. revised the paper. All authors discussed the results and commented on the manuscript. **Competing interests:** The authors declare that they have no competing interests. **Data and materials availability:** All data needed to evaluate the conclusions in the paper are present in the paper and/or the Supplementary Materials.

Submitted 12 August 2024
Accepted 4 December 2024
Published 8 January 2025
10.1126/sciadv.ads4038